



# Numerical investigation of internal flow characteristics in a mixed-flow pump with eccentric impeller

Wei Li<sup>1,2</sup> · Leilei Ji<sup>1</sup> · Weidong Shi<sup>3</sup> · Ling Zhou<sup>1</sup> · Ramesh Agarwal<sup>4</sup> · Elemam Mahmouda<sup>1</sup>

Received: 3 April 2020 / Accepted: 28 July 2020 / Published online: 10 August 2020  
© The Brazilian Society of Mechanical Sciences and Engineering 2020

## Abstract

In order to study the internal flow fields of mixed-flow pump with eccentric impeller, the numerical simulation and experiment have been conducted based on the dynamic sliding multi-region method. During simulation, the impeller domain has been separated by three sub-domains to apply the whirl effect. The pressure, turbulent kinetic dissipation and streamline distribution in the tip clearance were analyzed. The results show that the energy performance of calculation is basically consistent with the experimental results, which indicates the accuracy of energy performance prediction. The efficiency and head at the design flow condition drop about 20% and 11%, respectively, when  $e=0.5$  mm. The circumferential pressure distribution of impeller inlet and outlet is influenced greatly by the eccentric impeller, but the middle part of impeller suffered little effects as a result of the rotation effect of impeller. When the impeller is eccentric, the tip leakage flow and tip leakage vortex (TLV) are restrained at small tip clearance but enhance at large tip clearance. The angle between the TLV core and blade rim also increases at large tip clearance but decreases at small tip clearance. More energy has dissipated in the first half part of impeller channel within tip region, and the impacting depth increases with the increase in eccentricity, which affect the inlet flow fields of impeller at large eccentricity. The turbulent kinetic dissipation and hydraulic losses increase with the increase in eccentricity, which is the main factor for the decrease in pump efficiency.

**Keywords** Mixed-flow pump · Eccentricity · Dynamic sliding multi-region (DSMR) · Tip leakage flow

## 1 Introduction

The Alford effect was firstly noticed by Alford [1] in the field of axial flow gas turbine. When the impeller rotates with eccentricity, the blade tip clearance is unevenly distributed in the circumferential direction that increases the blade loading and generating a perpendicular force on the impeller [2].

Some literature also focuses on the measurement of Alford's force, e.g., Vance [3], Urlichs [4] and Laudadio [5]. Due to the rotor whirl and self-vibrations of impeller, the end shell is more likely to be hit by the impeller blade rim and be bruised and restrained [6]. Further, this phenomenon has been found in turbine by Jeong [7] and in compressor by Kang [8]. However, in the pump fields, the Alford effect is seldom focused.

The mixed-flow pumps are widely used in many fields as a kind of common hydraulic machinery benefiting from its high flow rate and moderate head [9]. But it is equipped with unshrouded impeller and the Alford effect resulting from the asymmetric fluid exciting force is obvious in actual operation [10, 11]. Thus, it is necessary to study the flow mechanism and flow field characteristics of mixed-flow pump with non-uniform tip clearance. In recent years, with the rapid improvement of CFD (computational fluid dynamics) software, the internal flow fields of mixed-flow pump under stable flow rate conditions are well predicted by many scholars, such as Yun [12], Yabin [13] and Zhou [14–16]. However, there exist many

---

Technical Editor: Daniel Onofre de Almeida Cruz.

✉ Wei Li  
lwjiangda@ujs.edu.cn

- <sup>1</sup> National Research Center of Pumps, Jiangsu University, Zhenjiang, People's Republic of China
- <sup>2</sup> Institute of Fluid Engineering Equipment, JITRI, Zhenjiang 212009, Jiangsu, People's Republic of China
- <sup>3</sup> College of Mechanical Engineering, Nantong University, Nantong 226019, People's Republic of China
- <sup>4</sup> Department of Mechanical Engineering and Materials Science, Washington University in St. Louis, St. Louis, MO 63130, USA

limitations for the prediction of unsteady flow fields of mixed-flow pump with eccentric impeller. At this condition, the impeller has whirl speed and the fluid domain cannot be divided as a fixed simulation domain by the ordinary static grid. Although the dynamic mesh can effectively solve this problem of the computational domain boundary [17, 18]. However, the dynamic mesh technology in pump is not developed enough until now, so this method could only predict the 2D flow field [19] or some simple 3D flow field [20]. In fact, the mesh is a key factor in simulating the internal flow fields of complex structure [21]. For the simple steady flow, the mesh could be refined to improve the accuracy of iteration, which is investigated and proved by Niu et al. [22–24]. But, for some complex flow fields which are attempted by Shafae [25], Adam [26] and Xiong [27], both of the mesh quality and interval time after mesh reconstruction could not be work out effectively.

When the mixed-flow pump runs with eccentric impeller, the internal flow field is extremely complicated and the flow in the tip is more difficult to predict due to the whirl motion of impeller. For symmetric tip clearance, the tip flow fields of mixed-flow pump have been investigated for a long time [28–31]. For instance, using numerical simulations and experimental tests, Bart et al. [32] founded that the unsteady hydraulic performance of mixed-flow pumps is not only affected by the tip clearance but also influenced by the unsteady rotating of the impeller. Goto et al. [33] numerically analyzed the interaction between the secondary flow and jet-wake flow in the mixed-flow pump without a cover plate. The results indicated that the backflow caused by tip leakage flow (TLF) is the main reason for the thickening of the boundary layer and the deterioration of the entire flow field. Based on PIV technique and SST  $k-\omega$  turbulence model, Masahiro et al. [34] focused on the mixed-flow leakage eddy at the  $0.6Q_{des}$  and its effect of the unsteady flow, also discussing the effect of grid number on the leakage flow velocity. Li et al. [35] found that the non-uniform tip clearance in the mixed-flow pump has greatly disturbed at the end wall of flow field and makes the leakage flow and the secondary flow increasing. Also, the hydraulic losses increase a lot due to the turbulent kinetic energy dissipation intensified with the increase in eccentric distance. Li et al. [36, 37] investigated the pressure pulsation characteristic at different monitoring locations and the cause of the unstable flow inside the pump. Jin et al. [38] studied the effects of different operating conditions, rotational speed and monitoring position on the time domain and frequency domain characteristics of the internal pressure pulsation in the mixed-flow pump. Till now, a lot of restrictions of the dynamic mesh technology to get an accurate prediction of the internal flow field and the energy performances of mixed-flow pump with

eccentric impeller, so a new calculation model should be set up.

In this paper, based on of the former investigation about the internal flow and shaft vibration [39, 40], the dynamic sliding multi-region (DSMR) method is established to study the instability flow characteristics in the vane-type mixed-flow pump with eccentric impeller. By using the standard  $k-\epsilon$  model, the energy performance in the mixed-flow pump is predicted and compared with the experiment results. Furthermore, the circumferential pressure, circumferential turbulent kinetic energy and streamlines distribution of the blade rim are investigated.

## 2 Simulation model

### 2.1 Three-dimensional solid modeling

The main objective of this research is to investigate a low specific speed mixed-flow pump with guide vane. The pump model component sections from the inlet to the outlet section of the annular volute chamber are shown in Fig. 1, and the parameters of the pump are listed in Table 1. The mixed-flow pump and the impeller inlet, guide vane, volute and outlet were modeled by Pro/E software. The three-dimensional solid modeling of the mixed-flow pump was obtained after assembly.

### 2.2 Impeller whirling motion model

Considering the eccentric impeller, when the impeller rotates, there will also be positive or negative whirl motion in the process of rotation due to the eccentricity between the center axes of the impeller and the chamber [41]. Therefore, the flow field simulation not only considered the impeller rotation but the whirl motion as well. The impeller whirl model [42] was introduced as shown in Fig. 2, where  $e$  is an eccentricity of the mixed-flow pump impeller and adjusted as 0 mm, 0.3 mm and 0.5 mm.

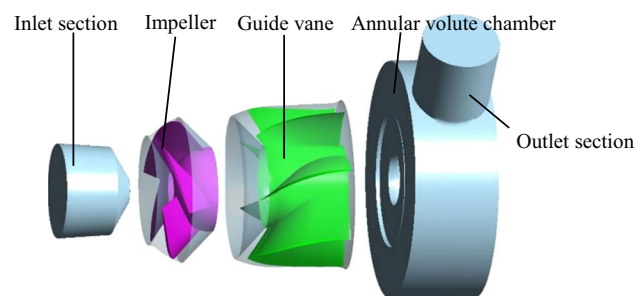
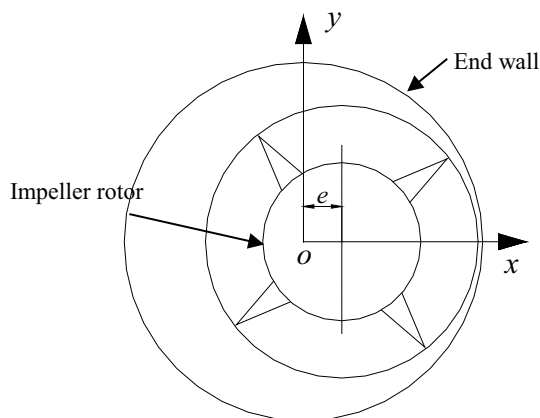


Fig. 1 Mixed-flow pump model

**Table 1** Parameters of mixed-flow pump model

<i>Impeller</i>		
Number of blades	$Z$	4
Inlet radius	$R_1$	92.6 mm
Outlet radius	$R_2$	121.6 mm
Inlet blade angle	$\beta_1$	53.5°
Outlet blade angle	$\beta_2$	58.4°
Tip clearance of impeller	$t$	0.8 mm
<i>Guide vane</i>		
Number of blades	$Z_d$	7
Inlet radius	$R_3$	133.3 mm
Outlet radius	$R_4$	140.9 mm
Inlet blade angle	$\alpha_3$	24.0°
Outlet blade angle	$\alpha_4$	26.0°
<i>Design operating point</i>		
Rated flow rate	$Q_{des}$	380 m <sup>3</sup> /h
Rated speed	$n$	1450 r/min
Rated head	$H$	6 m
Specific speed	$n_s$	480



**Fig. 2** Schematic diagram whirlling motion model

### 3 Dynamic sliding multi-region method

#### 3.1 Governing equations and turbulence models

The standard  $k-\epsilon$  model based on the Reynolds-averaged N-S equation has been widely applied in engineering calculations and the numerical prediction results, which have been verified by good agreements with the experimental results [43, 44]. Therefore, in this research, the standard  $k-\epsilon$  turbulence model is mainly used to study the internal flow characteristics in the mixed-flow pump with eccentric impeller. Assuming that the fluid is incompressible, the constraint equation of the turbulent kinetic energy  $k$

and the dissipation rate  $\epsilon$  in the standard  $k-\epsilon$  two-equation model is

$$\frac{\partial}{\partial t}(\rho k) + \frac{\partial}{\partial x_j}(\rho k u_j) = \frac{\partial}{\partial x_j} \left[ \left( \mu + \frac{\mu_t}{\sigma_k} \right) \frac{\partial k}{\partial x_j} \right] + G_k + G_b - \rho \epsilon - Y_M + S_k \tag{1}$$

$$\frac{\partial}{\partial t}(\rho \epsilon) + \frac{\partial}{\partial x_j}(\rho \epsilon u_j) = \frac{\partial}{\partial x_j} \left[ \left( \mu + \frac{\mu_t}{\sigma_\epsilon} \right) \frac{\partial \epsilon}{\partial x_j} \right] + C_{1\epsilon} \frac{\epsilon}{k} (G_k + C_{3\epsilon} G_b) - C_{2\epsilon} \rho \frac{\epsilon^2}{k} + S_\epsilon \tag{2}$$

Thus, the turbulent viscosity coefficient is

$$\mu_t = \rho C_\mu \frac{k^2}{\epsilon} \tag{3}$$

where  $i, j$  are the tensor symbols;  $u_i$  is the speed component (m s<sup>-1</sup>);  $x_j$  is the displacement component (m);  $t$  is the time (s);  $\mu_t$  is the turbulent viscosity (Pa s<sup>-1</sup>);  $\rho$  is the fluid density (kg m<sup>-3</sup>);  $k$  is the kinetic energy (m<sup>2</sup> s<sup>-2</sup>);  $\epsilon$  is the dissipation rate (m<sup>2</sup> s<sup>-3</sup>);  $G_k$  is the turbulent kinetic energy caused by the average velocity gradient;  $G_b$  is the kinetic energy caused by buoyancy;  $Y_M$  is the effect of compressible turbulence pulsation on total dissipation rate;  $C_\mu, C_{1\epsilon}, C_{2\epsilon}, C_{3\epsilon}$  are the empirical constants;  $\sigma_k, \sigma_\epsilon$  are the Prandtl numbers corresponding to the turbulent kinetic energy  $k$  and the dissipation rate  $\epsilon$ ;  $S_k, S_\epsilon$  are user-defined source items;  $C_{1\epsilon} = 1.44, C_{2\epsilon} = 1.92, C_\mu = 0.09, \sigma_k = 1.0$  and  $\sigma_\epsilon = 1.3$ .

#### 3.2 Establishment of dynamic sliding multi-region model

Theoretically, the dynamic mesh technology is a more effective and accurate method to predict the internal flow fields of mixed-flow pump with eccentric impeller because the removable boundary resulting from the whirl motion of impeller could be solved by the mesh reconstruction. However, the dynamic mesh technology is not yet developed, and the mesh update speed cannot keep up with the impeller rotation speed. The mesh reconstruction model of dynamic mesh model is not a perfect way to simulate eccentric flow fields at this time, because the negative volume happens when the mesh deforms to a certain extent, which would make the calculation stop immediately and affect the accuracy of simulation [17, 45, 46].

Nowadays, with the improvement of CFD, moving reference frame (MRF) model gives us another way to solve this kind of problems [47]. It is a simple model for multiple zones, which are approximately steady state, and the individual cell zones can be assigned at different rotational speeds. At the interfaces between cell zones, a local reference frame transformation is performed to enable using variables flow in one zone to calculate fluxes at the boundary of the adjacent

zone. In this model, the stationary and sub-domains flow is governed by the stationary frame equations, while the moving sub-domains flow is governed by the MRF equations. In addition, the MRF model could be applied together with the mesh motion model which needs an assumption for solving the problem of impeller with eccentric impeller. The coordinate system of MRF is shown in Fig. 3, where  $v_t$  stands for the linear velocity and  $\omega$  stands for the angular velocity in a stationary reference frame. The moving system origin is located by the position vector  $r_0$  where the axis of rotation is defined by a unit direction vector  $a$  as follows:

$$\omega = \omega a \tag{4}$$

The fluid velocities can be transformed from the stationary frame to the moving frame using the following relation:

$$v_r = v - u_r \tag{5}$$

In the above equations,  $u_r = v_t + \omega \times r$  and  $u_r$  is the velocity of the moving frame relative to the inertial reference frame,  $v_r$  is the relative velocity (the velocity viewed from the moving frame),  $v$  is the absolute velocity,  $v_t$  is the translational frame velocity, and  $\omega$  is the angular velocity.

According to the dynamic sliding region (DSR) method, used in the pump start-up process, which was proposed by Li et al. [45] and Wang et al. [46], the DSMR method was proposed to numerically calculate the internal flow fields of an impeller with whirl rotation. The DSMR method uses the mesh motion model in ANSYS Fluent 15.0 instead of the mesh reconstruction model. Meanwhile, this method contains the MRF model in the calculation process, while the impeller rotation and whirl motion are solved perfectly.

During calculation, the rotation domain, namely the impeller domain, is divided by three separate regions by

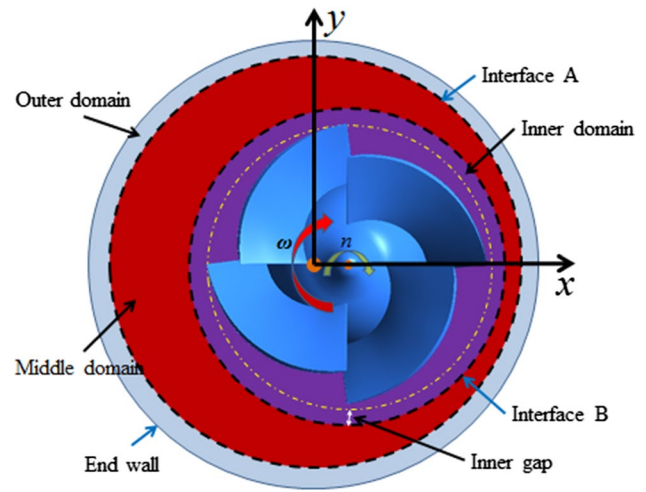
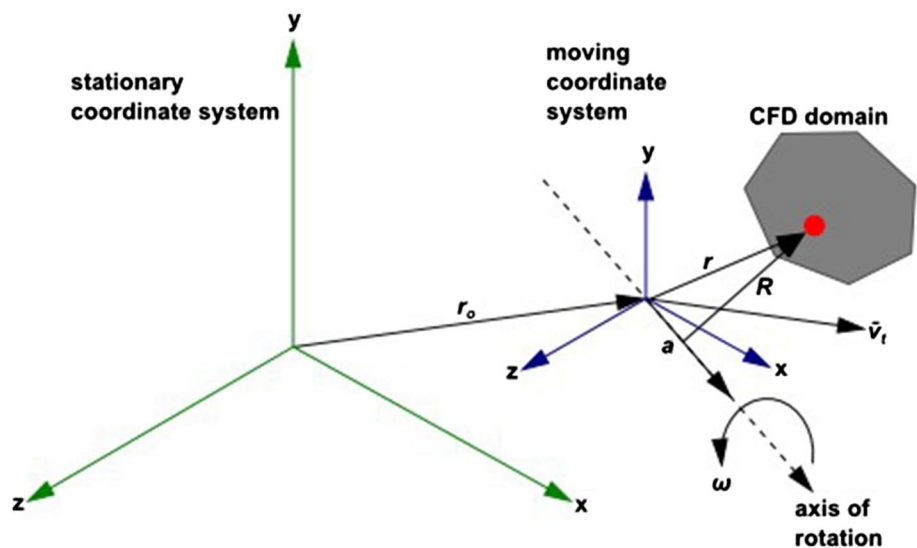


Fig. 4 Schematic diagram of DSMR method

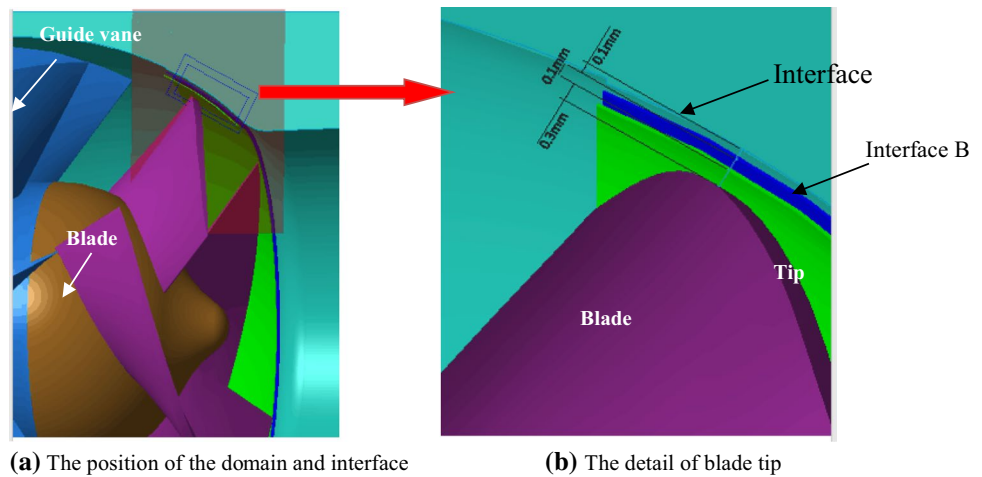
the DSMR method, which is shown in Fig. 4. The inner domain contains blades of impeller, the middle domain is generated to load the whirl effect, and outer domain includes the boundary layer of end wall. Through the Mesh Motion method, the middle domain is set as a reference to the inner domain. Each domain which is collected by the sliding interface and the data transmission of the non-overlapping mesh nodes between different domains is controlled by the interpolation method.

The original tip clearance of mixed-flow pump is 0.8 mm. The inner gap between the blade rim and interface B of inner domain is set as 0.3 mm uniformly when  $e$  is 0.3 mm. Similarly, the inner gap is set as 0.1 mm uniformly when  $e$  is 0.5 mm. The eccentricity is mainly controlled by the thickness of middle domain at different directions. When the eccentricity is 0.3 mm, the maximum thickness of middle

Fig. 3 Stationary and moving reference frames in simulation [46]



**Fig. 5** The position of the interface when eccentricity  $e$  is 0.3 mm



domain and the minimum thickness of middle domain, which is the distance of two bilateral interfaces of middle domain, are 0.7 mm and 0.3 mm, respectively. When the eccentricity is 0.5 mm, the maximum thickness of middle domain and the minimum thickness of middle domain are 1.1 mm and 0.1 mm, respectively. The thickness of outer domain, which is the distance between the external interface and shroud wall, is set as 0.1 mm uniformly. The position of the interface when eccentricity  $e$  is 0.3 mm is shown in Fig. 5.

### 3.3 Meshing and boundary conditions

The physical domain of mixed-flow pump includes the inlet pipe, impeller, guide vane, annular chamber and outlet pipe. And, the impeller domain is divided into three sub-domains so as to load the whirl effect. Therefore, the mesh generation of each domain or sub-domain should be conducted separately. The hexahedral mesh is employed to discretize these different domains with ICEM software. As the boundary layer of impeller blade surface should be considered in simulation, the mesh node near the impeller blade surface should be refined. The impeller blade surfaces should be surrounded by the mesh blocks, so the J/O-type topology is chosen for the mesh generation of impeller inner domain. The mesh nodes in the O mesh blocks near the blade surfaces are added to increase the mesh density. Further, to ensure that there is enough mesh within blade tip clearance, the mesh is also refined by controlling the density of mesh nodes within tip clearance. The  $y^+$  value of the blade rim is controlled within 100, which is shown in Fig. 6. Similarly, in order to refine the mesh node near the guide vane blade surfaces, the mesh generation of guide vane domain is also used the O-type topology to embrace the guide vane blade surfaces. As the structure of guide vane domain is simpler than impeller domain, the H/O topology is the final selection of whole guide vane domain. At last, all the separate parts

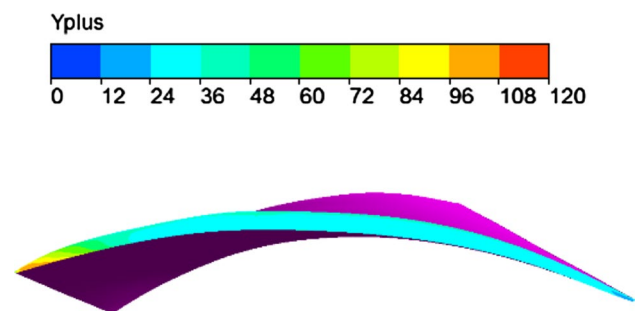


**Fig. 6**  $y^+$  of blade tip region

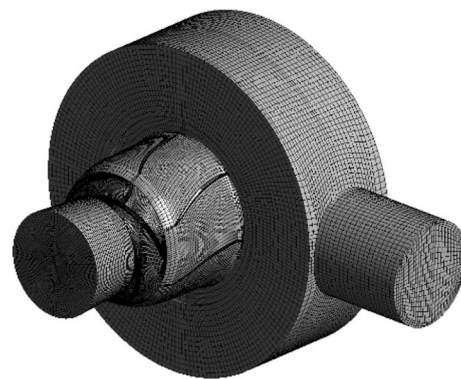


**Fig. 7** Mesh of the computational area

are assembled. The final mesh generation of whole mixed-flow pump is shown in Fig. 7. The impeller inner domain is set as a rotation domain automatically, and the whirl effect is applied in the middle domain by controlling its revolution speed. The whirl speed of different eccentric impeller is set as the same. The outer domain contains the boundary layer of end wall of mixed-flow pump. The inlet boundary of pump is used with velocity inlet which could be calculated by the flow rate conditions. The outlet boundary is set as the

pressure outlet, and the relative pressure is 30,000 Pa. The interfaces on both sides of impeller domain are set as slide interface to exchange the physical data of mesh nodes. Three sub-domains are also used this kind of interface. The other interfaces without movement are set as general interface. The wall roughness is not considered in this study. The time step is set as  $3.4483 \times 10^{-4}$  s, and the total time is set as  $8.138 \times 10^{-1}$  s. The convergence criterion is selected as  $10^{-4}$ .

### 3.4 Mesh sensitivity analysis

The mesh sensitivity analysis of simulation has been conducted when the rotational speed of mixed-flow pump is 1450 r/min. The same mesh topology is used, and the mesh quality is controlled when adjusting the identical mesh nodes. Figure 8 shows the pump head with different mesh densities by using the same control equations and boundary conditions when the eccentricity  $e$  is 0.3 mm.  $H$  represents the pump head. It is clear that the head increases gradually with the increase in mesh elements until 1.68 million. And, the head is changed within  $\pm 5\%$  which meets the mesh independent test requirements. Therefore, considering the accuracy and compute resource limitation of simulation, this kind of mesh elements is selected.

## 4 Energy performance experiment and verification

### 4.1 Experimental rig and test methods

A closed performance test device of mixed-flow pump is set up to verify the accuracy of the numerical simulation, which is shown in Fig. 9. The torque tachometer (ZJ-type) with accuracy class of 0.2 is used for the torque and the tachometric measurement, and the measurement range of torque meter is from 0 to 1000 N m. The turbine flow meter (LWGY-type) with accuracy class of 0.5 is set in the system to measure the flow rate, and the measurement range of flow

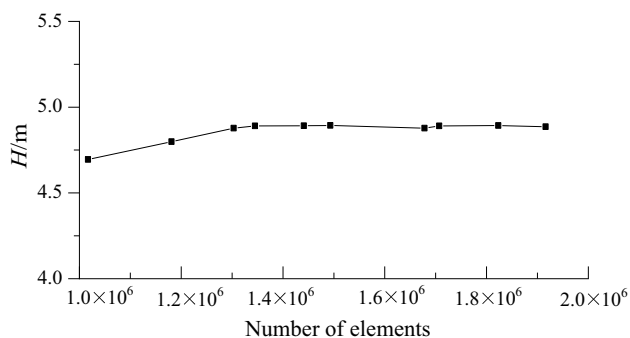


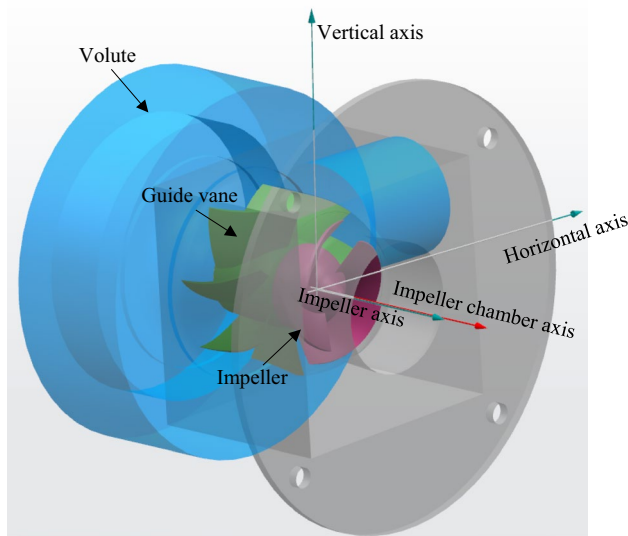
Fig. 8 Comparison of head under different mesh densities



Fig. 9 Experimental device. 1) motor; 2) torque meter; 3) mixed-flow pump; 4) pressure transmitter; 5) HSJ2010 hydraulic machinery comprehensive data acquisition instrument; 6) inlet valve; 7) turbine flow meter; 8) water tank

meter is from 0.4 to 1000 m<sup>3</sup>/h. The pressure transmitter (WT-1151) with accuracy class of 0.5% FS is equipped at the inlet and outlet of the mixed-flow pump to measure the inlet and outlet pressure. The measurement range of inlet pressure transmitter is from  $-100$  to 100 kpa, and the measurement range of outlet pressure transmitter is from 0 to 1000 kpa. The data have been transmitted to the HSJ2010 hydraulic machinery comprehensive data acquisition instrument after measurement, and then, it will be sorted and processed by computer. Finally, the change of operating point is achieved by regulating the opening of regulating valve on outlet pipe.

As we know, the existence of eccentricity and whirl motion leads to remarkable circumferential unbalance force when the impeller is rotating, whereas the force is difficult to be measured dynamically, and it may even cause the collision between impeller rim and impeller chamber end wall, leading to major accident. Thus, it is difficult to adjust the eccentricity directly. Further, the large eccentricity of impeller would cause the unsafety and instability of experiment. As we know, the position of impeller and impeller chamber is relative; thus, the eccentricity could be adjusted by changing the axial line of impeller chamber. Figure 10 shows the installation of impeller chamber and the chamber position. For example, the axial line of impeller and impeller chamber is coincident when the eccentricity is 0 mm, so the axial line of impeller chamber has not been changed at this situation. When the eccentricity is 0.3 mm, the eccentricity could be adjusted by changing the impeller chamber axis 0.3 mm away from the impeller axis. During the movement, the impeller chamber axis and the impeller axis should be kept parallelly. The movement of chamber could be divided into three stages. At the first stage, the impeller chamber moves



**Fig. 10** The installation of impeller chamber and the schematic diagram of chamber position

in the horizontal direction along the horizontal axis. Then, the size of the tip clearance at the horizontal direction is measured. Due to the eccentricity in the horizontal direction, the maximum and minimum tip clearance size occurs during the measurement. To keep the measurement accuracy, the tip clearance size in vertical axis should also be measured at last stage. And, the tip clearance size of two positions in this case should be the same. Likewise, the same procedure is conducted when the eccentricity is 0.5 mm.

Before the test, the opening of inlet value and outlet valve should be kept at the maximum. Once the energy performance begins, the power source of converter should be switched on, and the proper frequency should be set to ensure the pump speed is 1450 r/min. After that, the opening of outlet valve was gradually reduced, and the energy performance parameters of pump were recorded at different flow rate conditions. Then, when the fluid in the tube line was stabilized again, the repeated test was carried out.

For safety measurements, if the outlet valve was closed, the pump motor must be shut down.

### 4.2 Experimental results and verification

The energy performance of mixed-flow pump with different eccentricity is obtained, as shown in Fig. 11. As can be seen from the figure, the head and efficiency of  $e = 0$  mm are higher than the other two. With the eccentricity increases, the efficiency drops obviously and shows a significant negative correlation, and the efficiency at designed flow rate condition drops about 20% when eccentricity  $e$  is 0.5 mm. From  $0.4Q_{des}$  to  $0.6Q_{des}$ , the head descent is relatively small with the increase in eccentricity. But the head decreases significant with the increase in eccentricity from  $0.6Q_{des}$  to  $1.2Q_{des}$  and the head drops about 11% at designed flow condition when eccentricity  $e$  is 0.5 mm. The simulation head and efficiency have little difference with the results of experiment when the eccentricity is 0 mm and 0.3 mm. When the eccentricity is 0 mm, the head of simulation shows the same trend with experiment. But the head of simulation is slightly lower than the head of experiment at small flow rate when the eccentricity is 0.3 mm. The average head error is less than 5%, while the efficiency error is less than 3% under the situation of  $e = 0$  mm and  $e = 0.3$  mm. Even though the high error of head and efficiency between simulation and experiment exists when the eccentricity is 0.5 mm, it still meets the requirement of simulation, namely the maximum error of head or efficiency is less than 5%. When the eccentricity is 0.5 mm, the efficiency and head of experiment at design flow condition drop about 20% and 11%, respectively, compared with the results of  $e = 0$  mm. Therefore, the larger eccentricity of impeller means more hydraulic losses generating in mixed-flow pump during operation. Moreover, it is also known that the energy performance of mixed-flow pump with uniform tip clearance impeller is rather different from that with eccentric impeller. Hence, the new method provides higher accuracy for predicting the energy performance of mixed-flow pump with eccentric impeller. As a whole, the

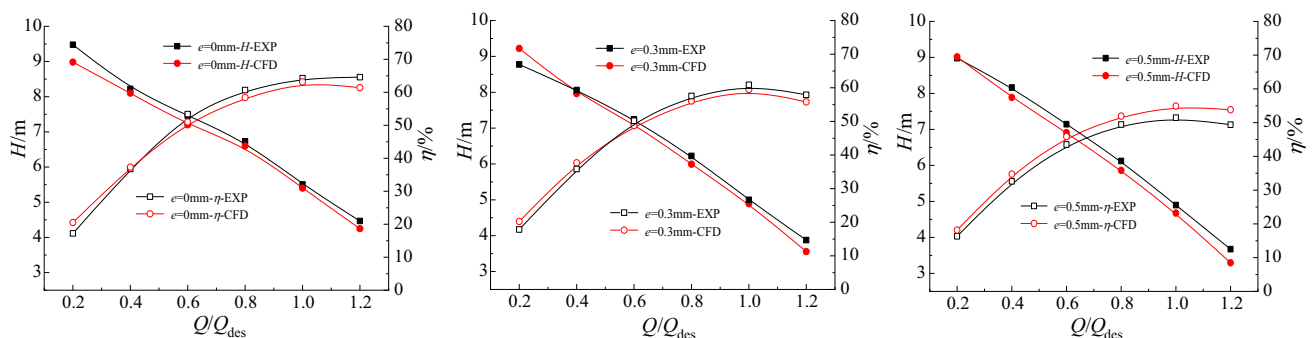


**Fig. 11** Comparison between experimental and simulation energy performance

energy performances of numerical calculation are still basically consistent with the experimental results and the overall error between numerical simulation and experiment is under tolerance, which indicates that the numerical calculation has a high accuracy.

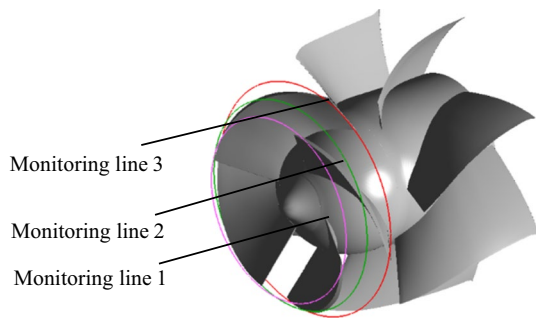


**Fig. 12** Position of monitoring lines

## 5 Analysis and discussion

### 5.1 Circumferential pressure distribution

In order to study the pressure distribution of tip region with different eccentricity, three monitoring lines are selected to analyze the pressure variation in the circumferential direction. All the monitoring lines are 0.2 mm away from the boundary wall vertically. The position of three monitoring lines is shown in Fig. 12.

The circumferential pressure of three monitoring lines is presented in Fig. 13. The  $x$ -axis shows the phase angle. It is the angle between points on monitor lines and point at minimum tip clearance of eccentric impeller, which starts at the minimum tip clearance of eccentric impeller and is presented in counterclockwise direction. On monitoring line 1, the circumferential pressure of four blade rim has the similar tendency and the distribution of highest or lowest

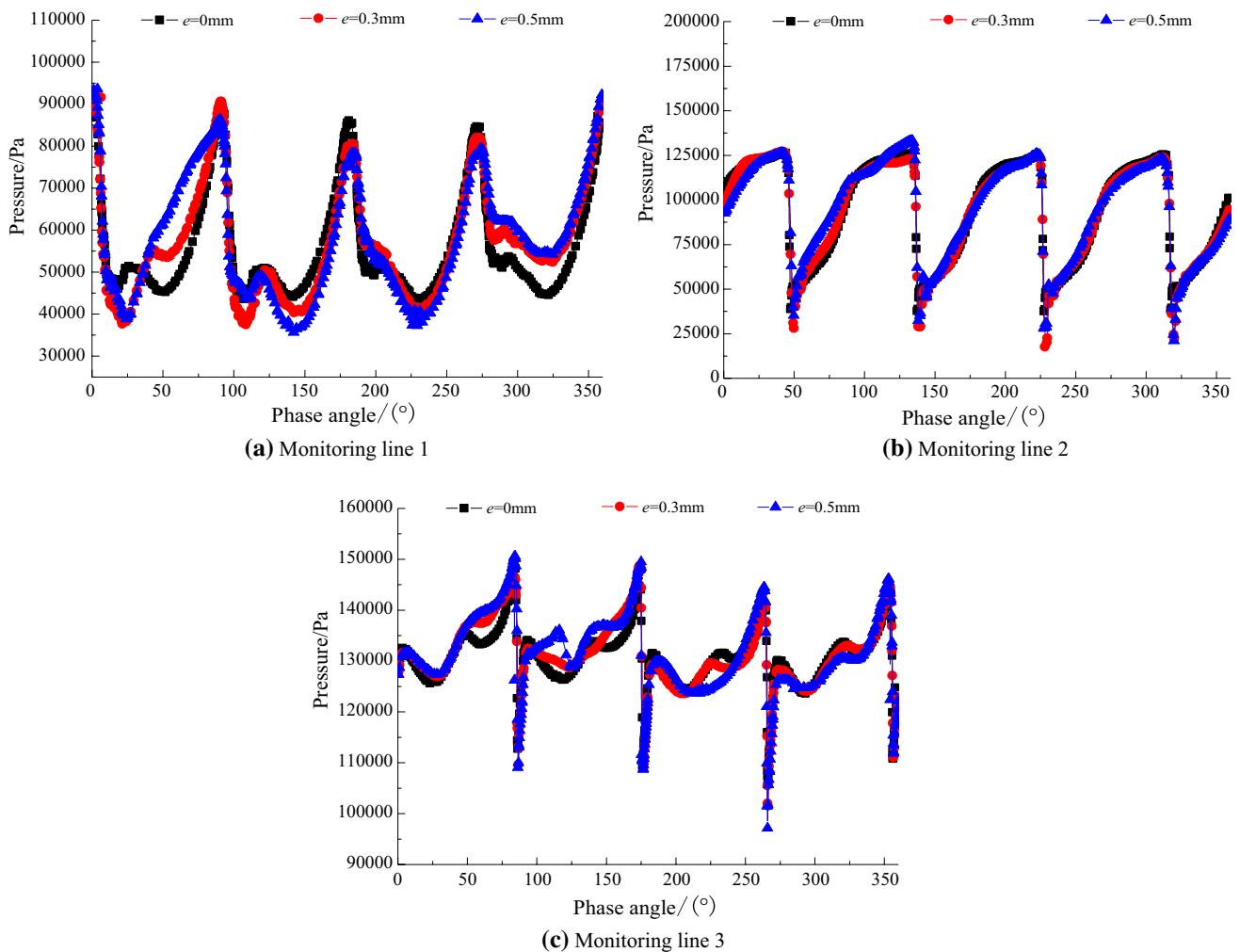


**Fig. 13** Circumferential pressure distribution at different monitoring lines



pressure amplitude is approximately the same as a result of the uniform tip clearance. When eccentricity is 0.3 mm, the circumferential pressure shows the non-uniform tendency in the circumferential direction. The lowest pressure value is lower than the non-eccentric impeller, while the overall pressure rises at the side of minimum tip clearance. When eccentricity is 0.5 mm, the circumferential pressure distribution is more different and asymmetric. With the increase of phase angle, the difference between the maximum pressure and minimum pressure decreases gradually, and the pressure shows a high positive slope curve on the eccentric side, which is obviously different from the non-eccentric impeller and the small eccentricity impeller. On monitoring line 2, the overall trend of circumferential pressure distribution of three kinds of impeller has little difference, but with the increase in phase angle, the highest pressure appears on eccentric side when eccentricity is 0.5 mm. On monitoring line 3, when the impeller is not eccentric, the circumferential pressure of blade rim has uniformly distributed. When eccentricity is 0.3 mm, the circumferential pressure distribution is similar with the non-eccentric impeller, but the highest pressure increases on the eccentric side. When eccentricity is 0.5 mm, the pressure varies along the blade rim and the circumferential pressure distribution is symmetric. The pressure value increases obviously near the eccentric side, and the highest and lowest pressure values appear together. The above analysis shows that the non-uniform rim clearance has a great influence on the impeller inlet and outlet pressure distribution, but it has a little effect on the pressure distribution in the middle region of impeller. The emergence of eccentricity changes the whole pressure field distribution inside impeller and affects the work efficiency of impeller, which has great effects on the energy performance of mixed-flow pump.

## 5.2 Circumferential turbulence energy distribution

Similarly, the circumferential turbulence energy distributions of three monitoring lines are obtained as shown in Fig. 14. When the impeller is not eccentric, the circumferential turbulence energy distribution of four blade rim is similar with the change of phase angle. However, the turbulence energy dissipation inside two eccentric impellers is higher than the non-eccentric one. On monitoring line 1, the turbulent kinetic energy dissipation of the flow field on the eccentric side is obvious, and the value of turbulent energy dissipation increases with the increase in eccentricity. On monitoring line 2, with the increase in eccentricity, the turbulent energy dissipation in the small clearance decreases, and the turbulent energy dissipation at large clearance increases. Moreover, the turbulent energy dissipation amplitude is higher, so it is the most serious area of energy loss. On monitoring line 3, the turbulent energy dissipation distribution of eccentric

impeller is more chaotic. When eccentricity is 0.5 mm, the maximum value of the turbulent energy dissipation is close to the middle section of the impeller and the energy has a severe loss. Therefore, the non-uniform rim clearance makes the velocity distribution in the clearance region varied; the turbulent energy dissipation and the hydraulic loss increases, which is the main cause of the drop of head and efficiency.

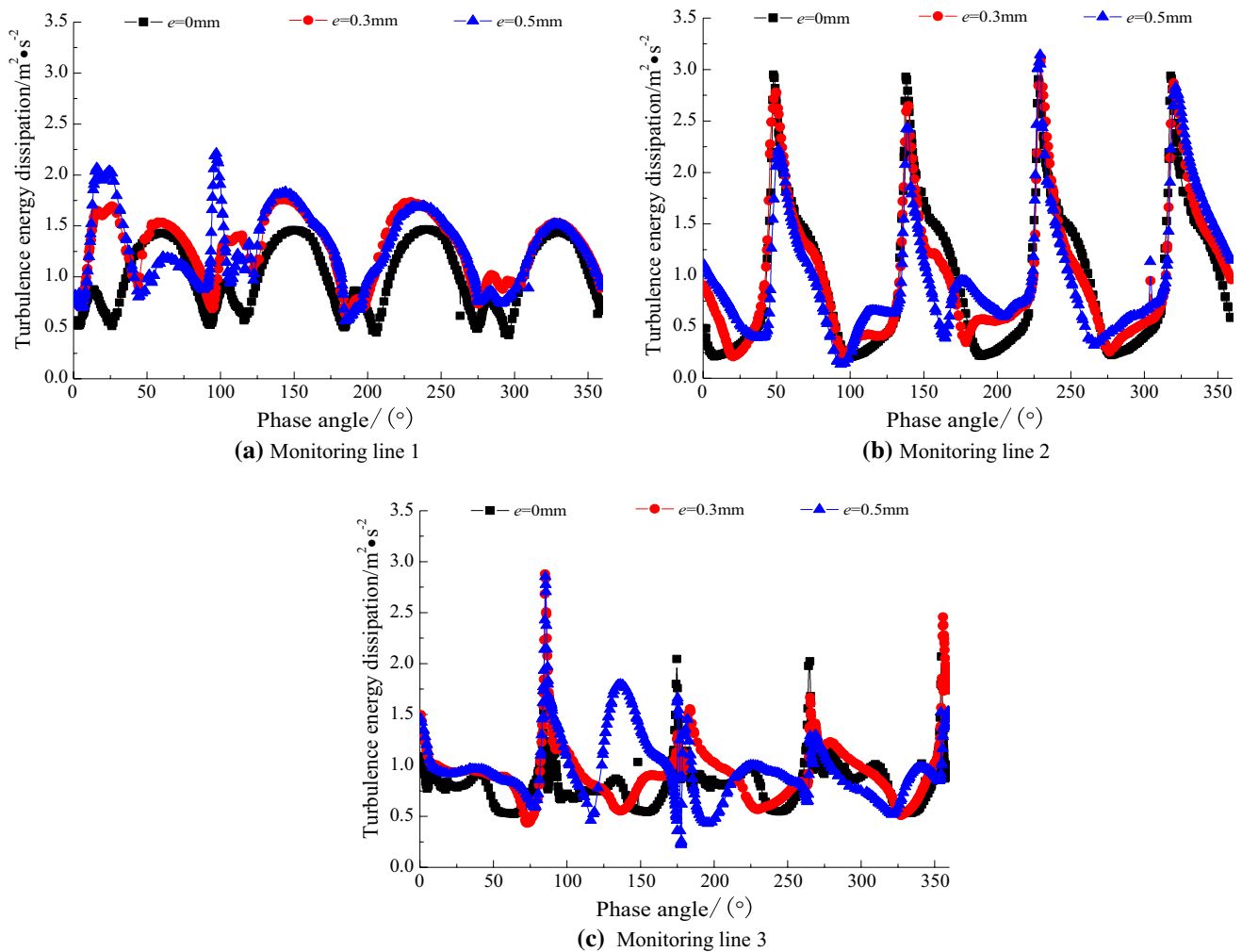
## 5.3 Streamline of tip region with different eccentricities

Figure 15 show the three-dimensional streamline of tip region under different eccentricities. The streamline of TLF is almost the same on the tip of four blades. The intensity of entrainment of tip leakage flow is high at the beginning of TLF which is near the local blade suction surface. Then, the TLF becomes weaker and a low velocity region occurs which is in front of next blade pressure surface. When the eccentricity exists in the impeller, the TLF of different blades changes a lot, and the streamline is much different of four blades at the same eccentricity. For instance, whatever the eccentricity is, the low velocity region becomes larger when the largest gap shows at the leading edge of blade, and it is more serious with the increase in eccentricity. The TLF of Blade C and Blade D at smallest gap decreases a lot, and the TLV shrinks to the local blade suction surface, which means the smaller impacted area in the impeller flow channel by TLF. Overall, the eccentricity could affect the circumferential TLF of impeller severely. With the augment of eccentricity, the unsteady characteristics of TLF and TLV are more obvious than the uniform tip clearance impeller.

## 5.4 Breaking of TLV under non-uniform tip clearance

As we know from above section, the leading edge of Blade A is at the largest tip clearance of eccentric impeller and the trailing edge of Blade C is at the smallest tip clearance of eccentric impeller. Therefore, to investigate the changes of TLF and TLV, the TLF of Blade A and Blade C has been studied in detail. Figures 16 and 17 shows the three-dimensional streamline of largest and smallest gap under two eccentricities. Five cross sections are equidistant set along the flow direction of TLF, and the vortex core distribution in cross sections is obtained and compared, which is shown in Figs. 18 and 19. The maximum and minimum tip clearance of different sections is at S1 and S10, respectively. On the several cross sections, the swirling intensity is shown. For the convenience of comparison, the range of swirling strength is in the same level.

It can be seen from Fig. 18, whatever the tip clearance is, the TLF forms TLV structure in the rear flow channel resulting from the entrainment effect. The velocity of



**Fig. 14** Circumferential turbulence energy dissipation distribution at different monitoring lines

TLF near the blade surface is high, but the flow velocity decreases gradually along the mainstream direction. At the large tip clearance, the strength of TLF and TLV increases significantly compared to the small gap flow fields under the same eccentricity. With the increase of eccentricity, the TLF increases, but the velocity in the TLF decreases. Meanwhile, the angle between the TLF and blade rim become larger, and the TLF interferes with the mainstream movement seriously. The TLF becomes more complex and unstable at downstream. Compared with the impeller when eccentricity  $e$  is 0.3 mm, the TLF increases and the influence on the main flow aggravate when eccentricity  $e$  is 0.5 mm, but the shear flow intensity weakens, which reduces the intensity of TLV. Furthermore, with the increase in eccentricity, the strength and influence of TLF gradually increase, and the interference effect of TLF on the mainstream continually enhances. The secondary flow in the flow channel deteriorates along the TLF as well. In Sects. 5 and 6, the TLF is squeezed by the main flow in the flow channel which causes the breaking of

TLV, generation of many secondary vortices and the chaos of flow fields. As shown in Fig. 17 (S4 and S5,  $e = 0.5$  mm), vortex A and vortex C come from the breaking components of tip leakage vortices; vortex B and vortex D are induced by secondary vortices. It is known that the secondary flow and chaotic flow affect the internal flow pattern and cause the velocity of fluid decline in the flow channels.

At the small tip clearance, with the increase in eccentricity, the scale of TLF shrinks gradually, and the vortex core moves closer to blade suction surface, which makes the angle between the TLF and blade rim smaller. Therefore, the interference effect of TLF to the main stream is weakened. With the increase of eccentricity, the TLF and TLV shrink further, and there is little fluid leaking from the tip clearance at largest eccentricity. Thus, the entrainment of TLF decreases and results in weaker effects in flow channel. Moreover, the TLV structure gradually attenuates and restrained near the blade leading edge, and then, the TLV structure disappears at blade trailing edge. The

**Fig. 15** Three-dimensional streamline of tip region under different eccentricities

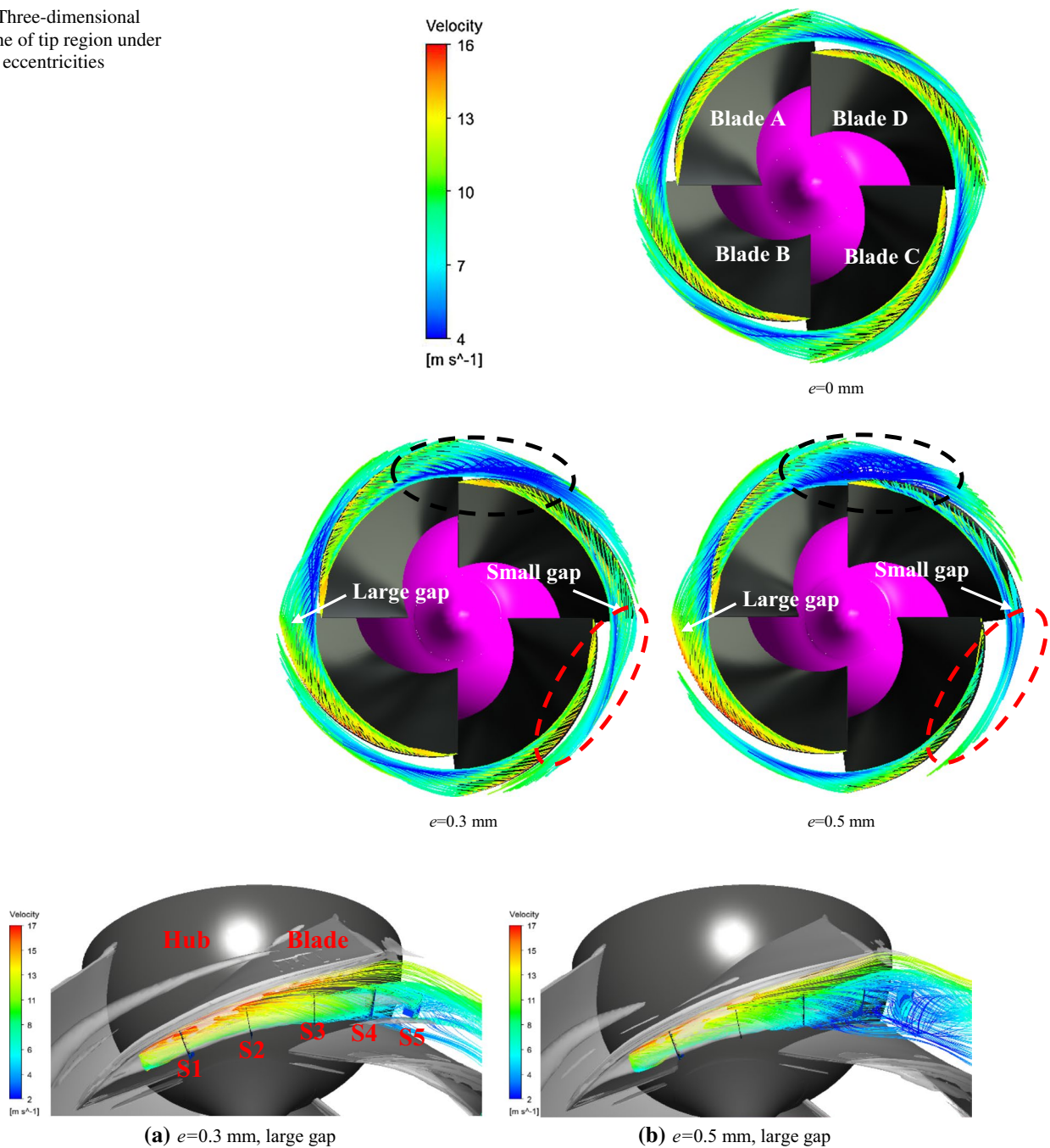


**Fig. 16** Streamline distribution of blade rim at large gap with eccentricity

swirling strength of TLF decreases along the TLV. Overall, the TLF is unstable under the eccentric situation and the circumferential distribution of TLF shows an unbalanced tendency. The angle between TLF and blade rim is influenced greatly by tip clearance, which determines the extent of interference of TLF with mainstream. The TLV shrinks further when the small tip clearance exists at the leading edge of blade, but it will break into small vortex and

secondary vortex in the rear impeller flow channels when the large tip clearance appears at the trailing edge of blade. Also, the eccentric impeller could deteriorate the internal flow and reduce the energy performance in mixed-flow pump. In order to weaken these adverse effects, eliminating or reducing the eccentricity of impeller could improve the pump performance.

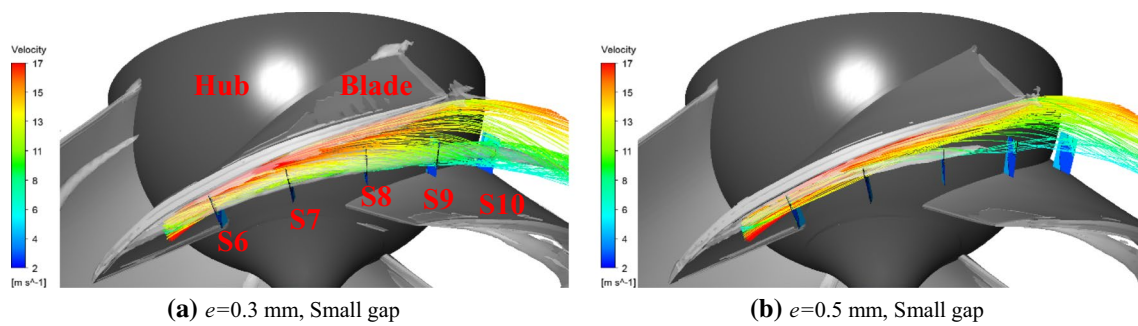


Fig. 17 Streamline distribution of blade rim at small gap with eccentricity

### 5.5 Circumferential distribution of turbulence kinetic energy with different eccentricities

To compare the effects of TLV, a series of sections are generated along the different blades. The circumferential distributions of turbulence kinetic energy with different eccentricities are shown in Fig. 20. For the convenience of comparison, the range of turbulence kinetic energy under different eccentricities is in the same level. When the tip clearance is uniform, the turbulence kinetic energy of TLV at various blade tip region is almost the same in the impeller channel. At the leading edge of blade, the entrainment effect of TLV is smaller than that at the trailing edge of blade. The angle between the blade chord and TLV is similar at four blades. When the impeller is eccentric, the turbulence kinetic energy caused by the TLF of Blade A, Blade B and Blade D increases a lot obviously, but it becomes smaller at Blade C. Thus, the non-uniform TLF in eccentric impeller could increase the energy losses in the tip region. It is known that the highest energy loss area of different eccentric impeller exists in front of Blade D, which is marked with dashed ellipse. In fact, it is corresponding to the most chaotic region on tip region. The unsteady flow region clearly affects the fluid flowing into the next blade tip clearance, which is another reason for the decrease in TLF at Blade D with the shrinkage of tip clearance. The turbulence kinetic energy along the blade at tip region shows high value which indicates much more energy have dissipated in the first half part of impeller channel. Compared with the TLV angle of different blade of eccentric impeller, the angle diminishes at Blade C and Blade D. Despite the angle change little at the front part of Blade A and Blade B, it shows a trend away from the blade surface at the end part of Blade A and Blade B. Therefore, the tip vortex trajectory along the blade chord also changes under eccentric impeller. Overall, the turbulence kinetic energy would increase a lot with the augment of eccentricities, which is the main reason for the drop of pump efficiency.

### 5.6 Impacting depth of TLF with different eccentricities

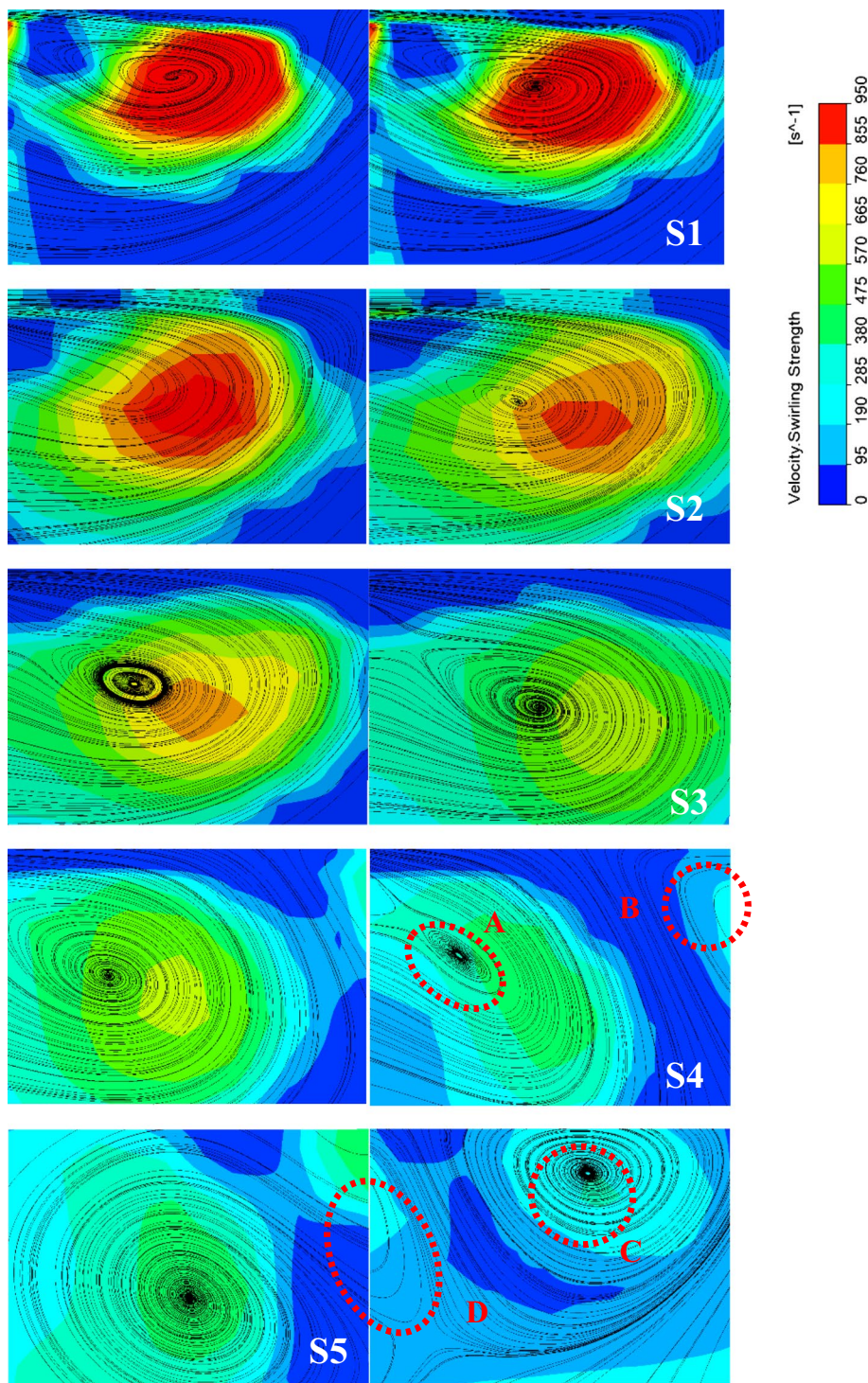
To contrast the impact depth of TLF and TLV under different eccentricities, the pressure of different span curves is collected. In order to eliminate the effect of location, the pressure data have been normalized with the local average pressure and the impeller parameters, which is shown as Eq. (5),

$$C_p = \frac{p - \frac{\sum p}{N}}{\frac{1}{2} \rho u_2^2} \quad (6)$$

where  $p$  is the local static pressure, Pa;  $u_2$  is the peripheral velocity of the impeller outlet, m/s; and  $\rho$  is the density of water, 1000 kg/m<sup>3</sup>.

Figure 21 shows the pressure coefficient  $C_p$  curve of 50% span, 75% span, 95% span and tip surface surrounding the blade surface with different eccentricity. In this figure,  $Z$  represents the distance along the shaft. When the impeller is uniform, the pressure coefficient  $C_p$  of four blades is almost the same, namely the curve structure at the same span surface is similar. When the impeller is eccentric, the pressure curve has been greatly affected. For instance, with the increase in eccentricity, the pressure coefficient of Blade B pressure surface decreases a lot at the middle of tip surface, which is marked with black dashed ellipse. In fact, comparing the pressure coefficient curve between non-eccentric impeller and 0.3 mm eccentricity impeller, the curve of 50% span, 75% span and 95% span surface has not been impacted much, but the curve of tip surface is different. It indicates that the impacting depth of TLF is relatively shallow. However, at large eccentricity, the pressure curve structure of Blade D at 75% span, 95% span surface and tip surface is rather different from the others, which means the impacting depth of TLF would also be changed seriously by higher eccentricity, where the impacting depth of TLF means the straight-line distance from impeller chamber

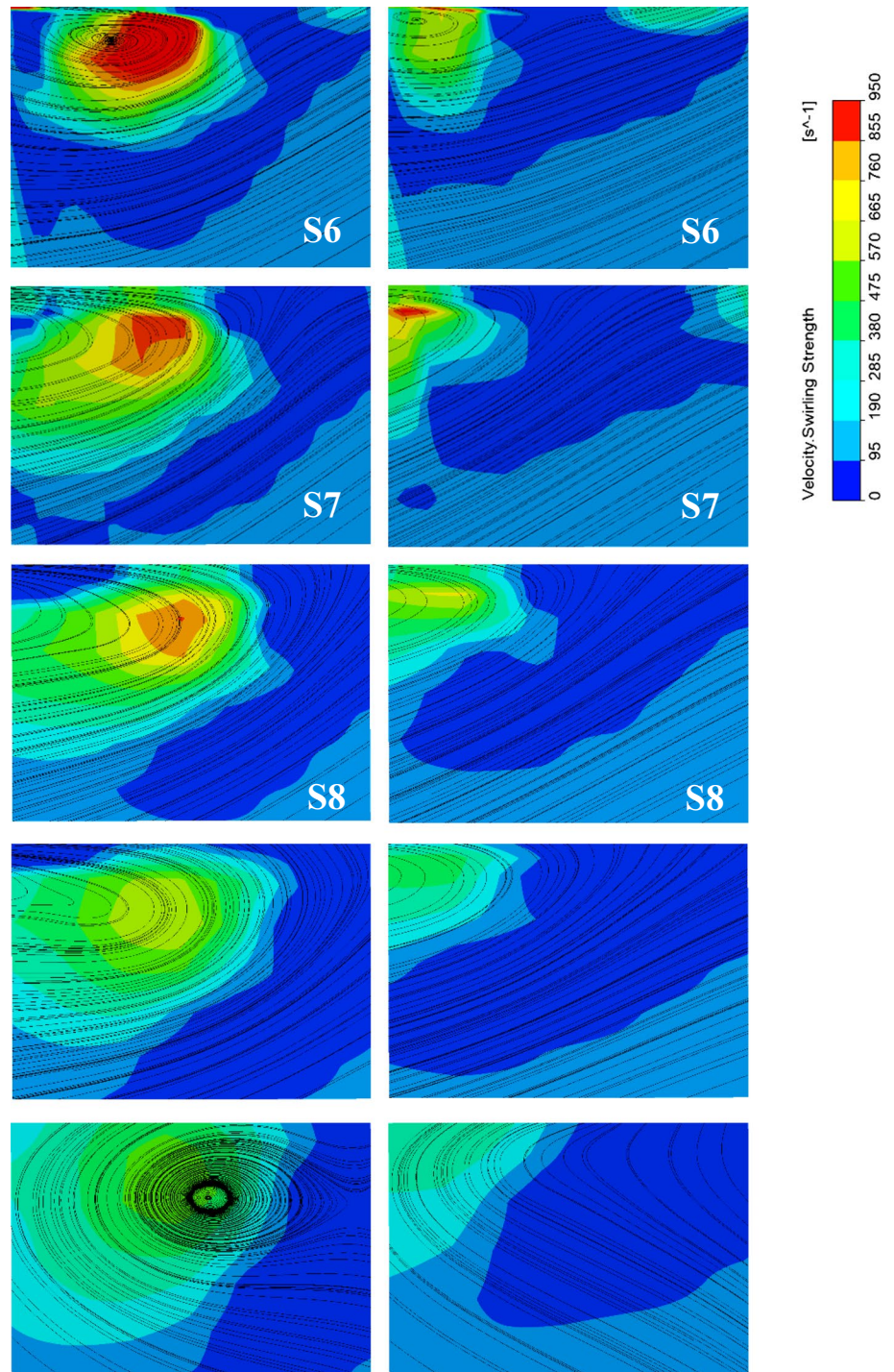
**Fig. 18** The streamline and swirling strength distribution of different monitoring sections at large gap. The left column is the results of  $e=0.3$  mm, and the right is the results of  $e=0.5$  mm



end wall to the position where it is impacted by the TLF. Simultaneously, at the leading part of blades, the pressure coefficient curve on 75% span and 95% span surface also changes which illustrates that large eccentricity would also impact the inlet flow fields of impeller at tip region. This is corresponding to the high energy loss dissipating area shown above. At 50% span surface of large eccentricity impeller,

the pressure coefficient curve does not change much which illustrates that the impacted region by the non-uniform tip clearance concentrated on the upper half part of impeller channels. Therefore, the eccentricity of impeller would also lead to the wider impacted region of flow fields in impeller channels, which makes more energy losses in the upper flow fields of impeller.

**Fig. 19** The streamline and swirling strength distribution of different monitoring sections at small gap. The left column is the results of  $e=0.3$  mm, and the right is the results of  $e=0.5$  mm



## 6 Conclusions

In this study, based on the simulation and experiment, the internal flow fields of a mixed-flow pump with eccentric impeller are investigated. The MRF with the DSMR method is employed, and some findings are as follows:

1. The error of head and efficiency meets the requirements of simulation under designed flow rate condition, which indicates the accuracy of energy performance prediction. At designed flow rate condition, the efficiency drops about 20% and head drops about 10% when  $e=0.5$  mm, compared with the results of  $e=0$  mm. The uniform

**Fig. 20** Circumferential distributions of turbulence kinetic energy with different eccentricities

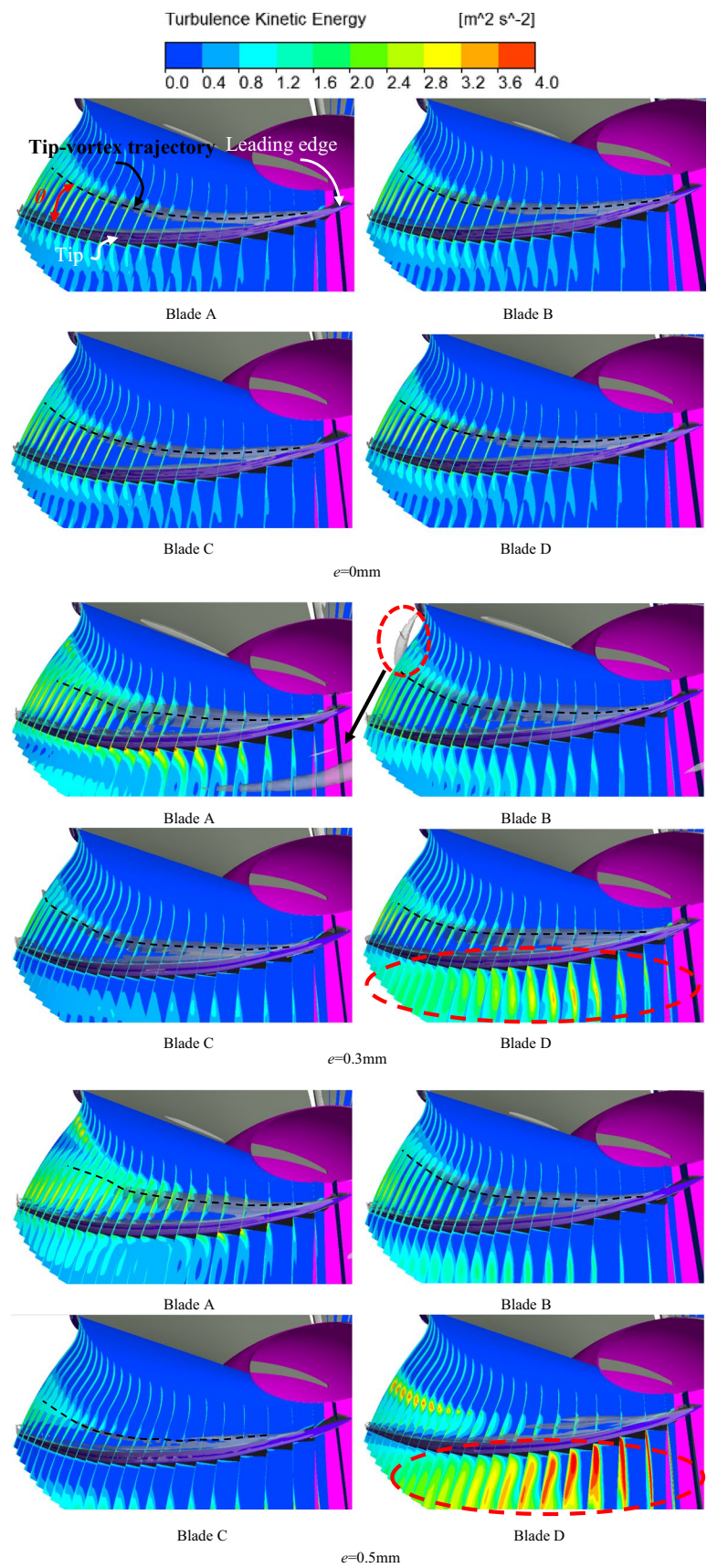


**Fig. 21** Pressure coefficient distribution of 50% span, 75% span, 95% span and tip surface surrounding the blade surface with different eccentricities

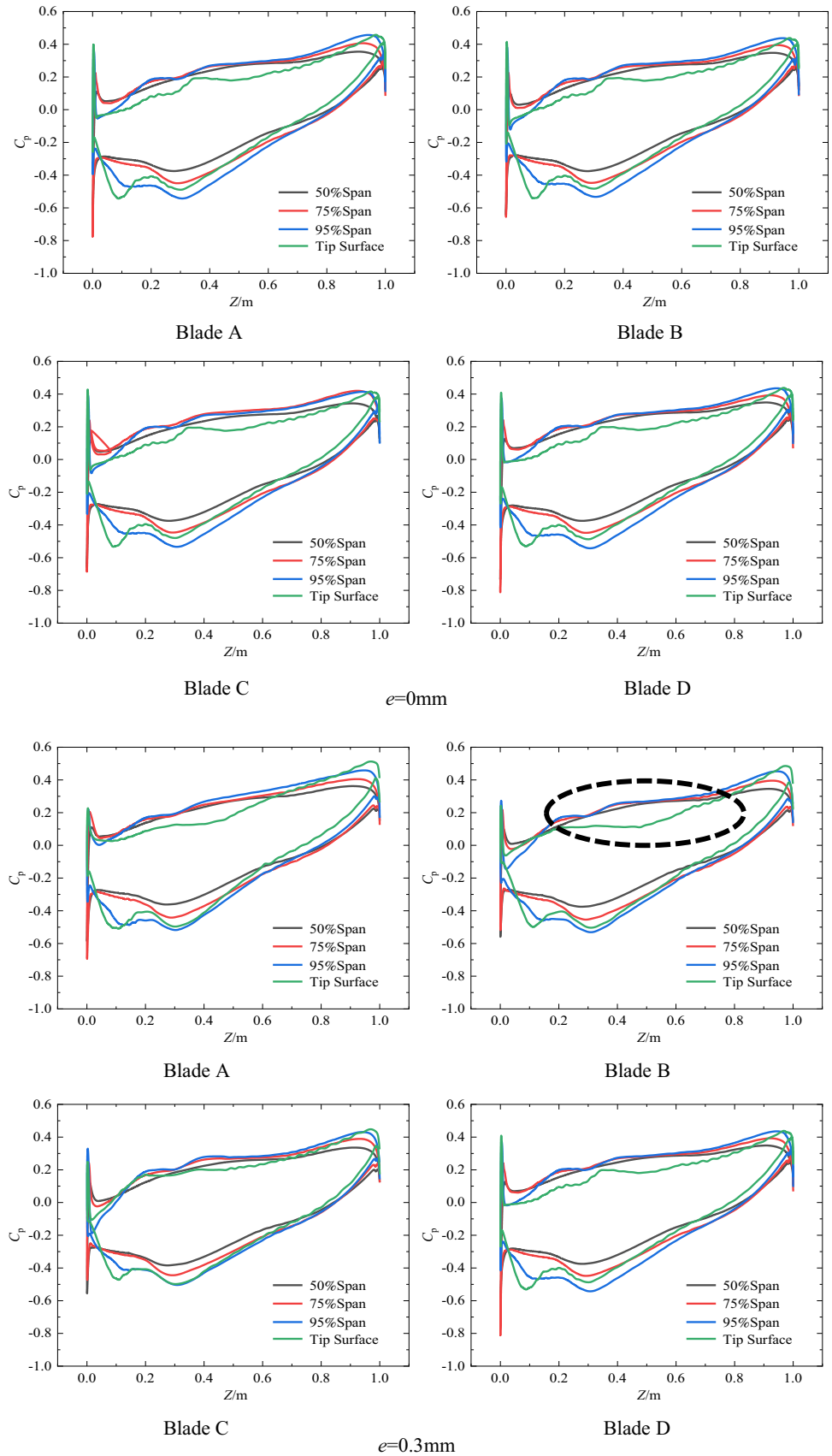
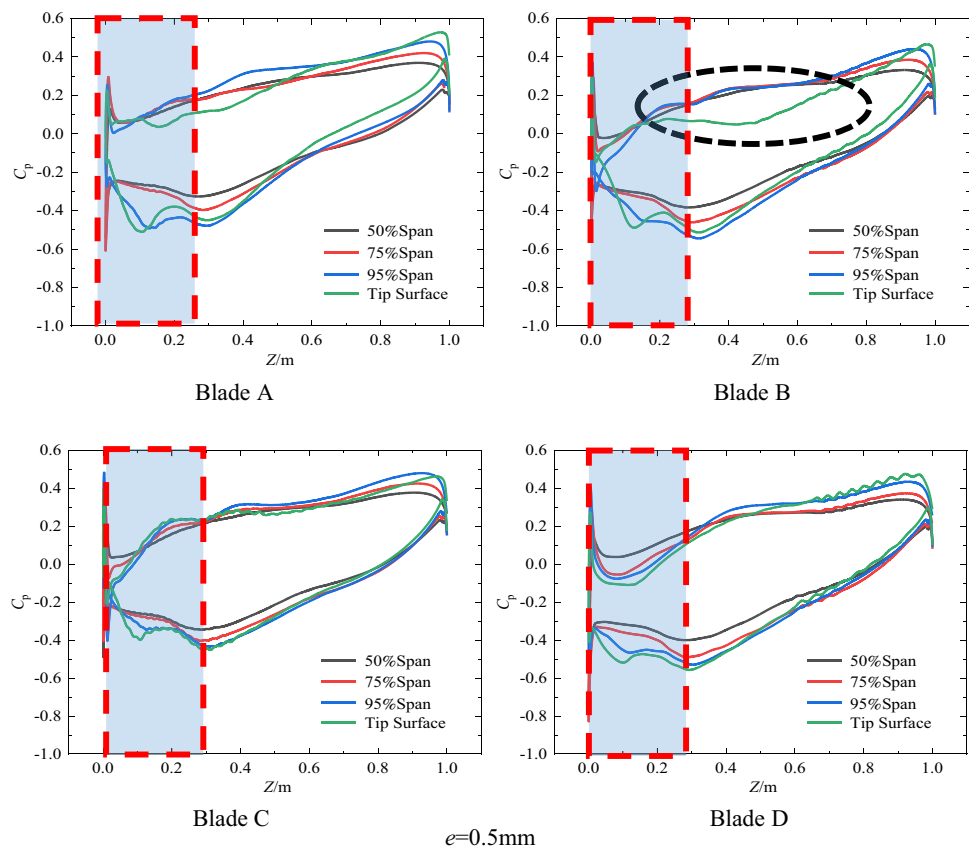




Fig. 21 (continued)



tip clearance of impeller would cause the increase in hydraulic losses of mixed-flow pump, and it is proportional to the eccentricity.

- The circumferential pressure distribution of impeller inlet and outlet is influenced greatly by the eccentric impeller, but the middle part of impeller suffered little effects as a result of the rotation effect of impeller. The turbulent energy dissipation within tip clearance in circumferential direction also increases because of non-uniform velocity distribution, which causes the increase in hydraulic losses as well. Thus, the emergence of eccentricity is the main reason for the head drop and efficiency reduction.
- When the impeller is eccentric, the strength of TLV and TLV increases at large tip clearance, which makes the angle between the TLV core and blade rim larger simultaneously. Further, more small secondary vortexes generate from the breaking component of TLV and block the impeller flow channel. However, the strength of TLV and TLV shrinks at small tip clearance, and the angle between the TLV core and blade rim decreases. Those trends become more severe with the increase in eccentricity.
- The highest energy loss area exists in front of the blade where it is located at smallest tip clearance, which could also account for the decrease in TLV of that blade. The

energy losses along the blade decrease which indicates much energy has dissipated in the first half part of impeller channel. The impacting depth of TLF increases with the increase in eccentricity, but it concentrates on the upper half part of impeller channels. The inlet flow fields of impeller at tip region, which is corresponding to the high energy loss area, would also be affected severely at large eccentricity.

In the near future, studies will be focused on the non-linear dynamic behavior of shaft system in the mixed-flow pump induced by the eccentric impeller. Besides, some effective method should be applied to the mixed-flow pump to improve the performance and reliable operation of mixed-flow pumps and widen its application as well.

**Acknowledgements** The work was sponsored by the National Natural Science Foundation of China (Nos. 51679111, 51979138), Key R&D Program Project in Jiangsu Province (BE2017126), Synergistic Innovation Center of Jiangsu Modern Agricultural Equipment and Technology (4091600014), PAPD, National Key R&D Program Project (No. 2017YFC0403703), Key R&D Program Project of Zhenjiang (No. SH2017049) and Scientific Research Start Foundation Project of Jiangsu University (No. 13JDG105), Postgraduate Research and Practice Innovation Program of Jiangsu Province (KYCX19\_1601).

## References

- Alford JS (1965) Protecting turbomachinery from self-excited rotor whirl. *J Eng Power* 87(4):333–343
- Thomas HJ (1958) Unstable natural vibration of turbine rotors induced by the clearance flow in glands and blading. *Bull De l'AIM* 71(11):1039–1063
- Vance J, Laudadio F (1984) Experimental measurement of Alford's force in axial flow turbomachinery. *J Eng Gas Turbines Power* 106(3):585–590
- Urlichs K (1976) Leakage flow in thermal turbo-machines as the origin of vibration-exciting lateral forces. *Ing. Arch. (West Germany)* 45(3):193–208
- Laudadio FJ (1984) Experimental measurement of Alford's force in axial flow turbomachinery. *J Eng Gas Turbines Power* 106:585
- Kim HS, Cho MH, Song SJ (2003) Stability analysis of a turbine rotor system with Alford forces. *J Sound Vib* 260(4):167–182
- Jeong E, Lee H-G, Park P-G et al (2008) Tip clearance effect on the performance of a shrouded supersonic impulse turbine. *J Propul Power* 24(6):1295–1300
- Kang Y-S, Kang S-H (2010) Prediction of the nonuniform tip clearance effect on the axial compressor flow field. *ASME J Fluids Eng* 132(5):9
- Ji L, Li W, Shi W et al (2020) Energy characteristics of mixed-flow pump under different tip clearances based on entropy production analysis. *Energy* 199:117447
- Li W, Ji L, Shi W et al (2016) Experimental study on orbit of shaft centerline of mixed-flow pump during starting time. *J Mech Eng* 52(22):168–177
- Li W, Li E, Ji L, Zhou L, Shi W, Zhu Y (2020) Mechanism and propagation characteristics of rotating stall in a mixed-flow pump. *Renew Energy* 153:74–92
- Yun X, Lei T, Yabin L, Shuliang C (2017) Pressure fluctuation and flow pattern of a mixed-flow pump with different blade tip clearances under cavitation condition. *Adv Mech Eng* 9(4):1–12
- Yabin L, Lei T, Hao Y, Yun X (2017) Energy performance and flow patterns of a mixed-flow pump with different tip clearance sizes. *Energies* 10(1):191
- Jiang X, Wang L, Zhou L, Li W, Wang C (2020) Transient response analysis of cantilever multistage centrifugal pump based on multi-source excitation. *J Low Freq Noise Vib Act Control* 2019:1–17
- Bai L, Zhou L, Jiang X, Pang Q, Ye D (2019) Vibration in a multistage centrifugal pump under varied conditions. *Shock Vib* 2019:2057031
- Bai L, Zhou L, Han C, Zhu Y, Shi W (2019) Numerical study of pressure fluctuation and unsteady flow in a centrifugal pump. *Processes* 7(6):354
- Huang S, Yang F, Guo J et al (2013) Numerical simulation of 3D unsteady flow in centrifugal pump by dynamic mesh technique. *Sci Technol Rev* 31(24):33–36
- Jiang F, Chen W, Wang Y et al (2007) Numerical simulation of flow field inside of centrifugal pump based on dynamics mesh. *Fluid Mach* 35(7):20–24
- Ortiz-Rivera I, Shum H, Agrawal A et al (2016) Convective flow reversal in self-powered enzyme micropumps. *Proc Natl Acad Sci* 113(10):2585–2590
- Kuron M, Stärk P, Holm C et al (2019) Hydrodynamic mobility reversal of squirmlers near flat and curved surfaces. *Soft Matter* 15:5908–5920
- Kuron M, Stärk P, Burkard C et al (2019) A lattice Boltzmann model for squirmlers. *J Chem Phys* 150(14):144110
- Niu R, Oğuz EC, Müller H et al (2017) Controlled assembly of single colloidal crystals using electro-osmotic micro-pumps. *Phys Chem Chem Phys* 19(4):3104–3114
- Niu R, Kreissl P, Brown AT et al (2017) Microfluidic pumping by micromolar salt concentrations. *Soft Matter* 13(7):1505–1518
- Lei QL, Ni R (2019) Hydrodynamics of random-organizing hyperuniform fluids. *Proc Natl Acad Sci* 116(46):22983–22989
- Shafae M, Mahmoudzadeh S (2017) Numerical investigation of spray characteristics of an air-blast atomizer with dynamic mesh. *Aerosp Sci Technol* 70:351–358
- Adam A, Pavlidis D, Percival JR et al (2016) Higher-order conservative interpolation between control-volume meshes: application to advection and multiphase flow problems with dynamic mesh adaptivity. *J Comput Phys* 321:512–531
- Xiong W, Cai CS, Kong B et al (2014) CFD simulations and analyses for bridge-scour development using a dynamic-mesh updating technique. *J Comput Civ Eng* 30(1):04014121
- Peraire J, Peiro J, Morgan K (1992) Adaptive remeshing for three-dimensional compressible flow computations. *J Comput Phys* 103(2):269–285
- Tan L, Zhiyi Yu, Yun X, Liu Y, Cao S (2017) Role of blade rotational angle on energy performance and pressure fluctuation of a mixed-flow pump. *Proc Inst Mech Eng Part A J Power Energy* 231(3):227–238
- Ji L, Li W, Shi W et al (2014) Numerical simulation of unsteady flow characteristics in mixed-flow pump with guide vanes. *Trans Chin Soc Agric Mach* 32(10):845–851
- Ji L, Wei L, Shi W (2019) Influence of tip leakage flow and inlet distortion flow on a mixed-flow pump with different tip clearances within the stall condition. *Proc Inst Mech Eng Part A J Power Energy* 234:433–453
- van Esch B, Cheng L (2011) Unstable operation of a mixed-flow pump and the influence of tip clearance. In: *ASME-JSME-KSME 2011 joint fluids engineering conference*, vol 1, Jan 01, 2011
- Goto A (1996) Study of internal flows in a mixed-flow pump impeller at various tip clearances using three-dimensional viscous flow computations. *ASME J Turbomach* 114(2):373–382
- Miyabe M, Furukawa A (2009) Hideaki Maeda and Isamu Umeki. Investigation of internal flow and characteristic instability of a mixed flow pump. In: *Proceedings of the ASME 2009 fluids engineering division summer meeting FEDSM2009*, Aug 2–6, 2009, Vail, Colorado USA, FEDSM 2009-78277
- Li W, Ji L, Shi W et al (2016) Numerical calculation of internal flow field in mixed-flow pump with non-uniform tip clearance. *Trans Chin Soc Agric Mach* 47(10):66–72
- Li Y, Li R, Wang X (2013) Numerical analysis of pressure fluctuation in low specific speed mixed-flow pump. *J Drain Irrig Mach Eng* 31(3):205–209
- Li Y, Li R, Wang X (2013) Numerical simulation of unstable characteristics in head curve of mixed-flow pump. *J Drain Irrig Mach Eng* 31(5):384–389
- Jin S, Wang Y, Chang S et al (2013) Pressure fluctuation of interior flow in mixed-flow pump. *Trans Chin Soc Agric Mach* 44(3):64–68
- Li W, Ji L, Shi W et al (2016) Influence of different flow conditions on rotor axis locus of mixed-flow pump. *Trans Chin Soc Agric Eng* 32(4):91–97
- Li W, Yang Y, Shi W et al (2015) Mechanical properties of mixed-flow pump impeller based on bidirectional fluid-structure interaction. *Trans Chin Soc Agric Mach* 46(12):82–88
- Chen S (2013) Study of fluid-induced forces in a centrifugal pump under given rotordynamic parameters. Jiangsu University, Zhenjiang
- Brennen CE, Acosta AJ (2006) Fluid-induced rotor-dynamic forces and instabilities. *Struct Control Health Monit* 13(1):10–26
- Li X, Liu C, Bo W et al (2014) Numerical simulation of oblique flow pump with single arc space vane based on CFX. *Water Resour Power* 4:175–179

44. Yang C, Gao Q, Li Y et al (2014) Application of different turbulence models in numerical simulation of the mixed-flow pump and its evaluation. *J Lanzhou Univ Technol* 40(5):51–55
45. Li Z (2009) Numerical simulation and experimental study on the transient flow in centrifugal pump during starting time. Zhejiang University, Hangzhou
46. Wang L, Li Z, Dai W et al (2008) 2-D numerical simulation of transient flow in centrifugal pump during starting time. *J Eng Thermophys* 29(8):1319–1322
47. Lawrence KL (2002) ANSYS® tutorial. Schroff Development Corporation, Mission

**Publisher's Note** Springer Nature remains neutral with regard to jurisdictional claims in published maps and institutional affiliations.